Radial Compression of Microtubules and the Mechanism of Action of Taxol and Associated Proteins

Daniel J. Needleman,*† Miguel A. Ojeda-Lopez,*† Uri Raviv,*† Kai Ewert,*† Herbert P. Miller,† Leslie Wilson,† and Cyrus R. Safinya*†

*Materials Department, Physics Department, and †Molecular, Cellular, and Developmental Biology Department, University of California, Santa Barbara, California 93106

ABSTRACT Microtubules (MTs) are hollow cylindrical polymers composed of $\alpha\beta$-tubulin heterodimers that align head-to-tail in the MT wall, forming linear protofilaments that interact laterally. We introduce a probe of the interprotofilament interactions within MTs and show that this technique gives insight into the mechanisms by which MT-associated proteins (MAPs) and taxol stabilize MTs. In addition, we present further measurements of the mechanical properties of MT walls, MT-MT interactions, and the entry of polymers into the MT lumen. These results are obtained from a synchrotron small angle x-ray diffraction (SAXRD) study of MTs under osmotic stress. Above a critical osmotic pressure, P_{cr}, we observe rectangular bundles of MTs whose cross sections have buckled to a noncircular shape; further increases in pressure continue to distort MTs elastically. The P_{cr} of $\sim$600 Pa provides, for the first time, a measure of the bending modulus of the interprotofilament bond within an MT. The presence of neuronal MAPs greatly increases P_{cr}, whereas surprisingly, the cancer chemotherapeutic drug taxol, which suppresses MT dynamics and inhibits MT depolymerization, does not affect the interprotofilament interactions. This SAXRD-osmotic stress technique, which has enabled measurements of the mechanical properties of MTs, should find broad application for studying interactions between MTs and of MTs with MAPs and MT-associated drugs.

INTRODUCTION

Microtubules (MTs) are hollow, cylindrical cytoskeletal polymers whose structural, mechanical, and polymerization properties are crucial for cell division, cell structure, and intracellular transport in eukaryotes. MTs are formed from $\alpha\beta$-tubulin protein heterodimers. The structure of the dimeric tubulin subunit is known (1) and high-resolution models of MTs are available (2). Tubulin dimers stack longitudinally into protofilaments that form the MT wall (Fig. 1). Protofilaments form sheets at the end of growing MTs (3). At the ends of shortening MTs, protofilaments curl and peel apart from each other, eventually detaching from the MT as highly curved oligomers (4). However, despite this detailed structural knowledge, the forces and interactions that control MT dynamics are not well understood. There is no comprehensive model for the unique and complex manner of MT polymerization, called dynamic instability, in which MTs stochastically switch between growing and shortening phases, but it is thought that the curvature of protofilaments and the interaction between protofilaments are two of the key microscopic determinants (5).

MT polymerization is strongly affected by solution conditions, such as the ionic strength (6) and the presence of drugs and MT-associated proteins (MAPs). Many anticancer drugs currently in use in clinical chemotherapy function by interfering with MT dynamics (7). For example, taxol, which is widely used to treat breast and ovarian cancer, prevents cell division by binding to and stabilizing MTs (8). However, the microscopic mechanism by which taxol affects MTs is unclear. It has been proposed that taxol stabilizes MTs by either increasing the lateral interactions between protofilaments (9) or by locking the protofilaments in a straight conformation (10). MAPs regulate dynamic instability in vitro (11) and in cells (12). A number of neurodegenerative diseases are associated with improper MAP-MT interactions (13). The microscopic mechanism by which distinct MAPs affect MT dynamics is not well understood. It is unclear if MT-stabilizing MAPs function by cross-linking tubulin dimers within a protofilament or between protofilaments, or if they change the protofilaments curvature. They may also cause a conformational change in tubulin or work by different mechanisms (14).

MTs are often organized into bundles in vivo. These bundles show a wide variety of internal organizations. In many instances the biological significance of MT bundle formation is unclear; for example, the role of MT bundles observed at the hillock region of nerve cells and also protruding along the axon are unknown (15). MT organization is directed by MAPs (16) in vivo. However, even though MAPs can bundle MTs in vitro (17) and in in vivo overexpression experiments (18), the mechanism of bundle formation remains controversial (19). It is unclear if MAPs directly cross-link MTs, act as spacers between MTs, or facilitate a preexisting attraction between MTs (19–21). Furthermore it is not known how these microscopic interactions between MTs, mediated by MAPs, could give rise to the MT bundles with different morphologies observed in vivo. The study of model systems should help to illuminate these issues.

The presence of inert macromolecules can lead to an effective attraction between particles in a manner that is well

Submitted December 7, 2004, and accepted for publication July 26, 2005.

Address reprint requests to Cyrus R. Safinya, E-mail: safinya@mrl.ucsb.edu.

0006-3495/05/11/3410/14 $2.00

doi: 10.1529/biophysj.104.057679

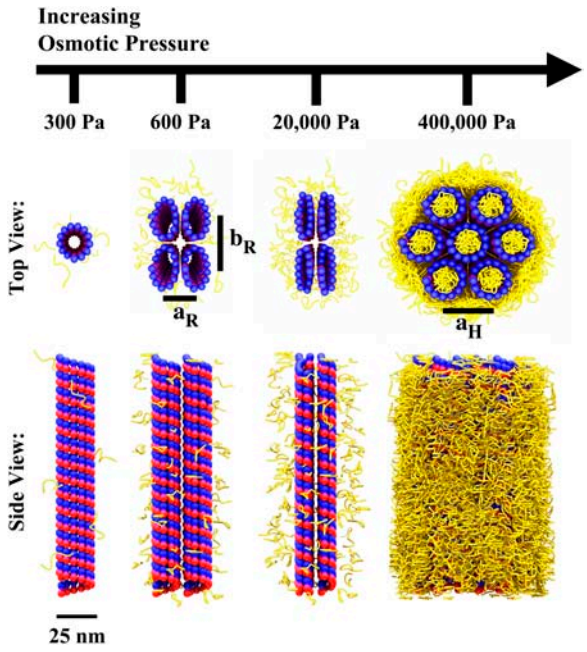

FIGURE 1 Schematic illustration of the MT phases observed. For <0.4% (wt/wt) 20 k PEO (corresponding to an osmotic pressure of 600 Pa), the MTs are undistorted and form a nematic. Above this concentration of 20 k PEO, the MTs buckle to a noncircular cross section and form bundles with rectangular symmetry. The MTs distort further as the osmotic pressure increases. At 5% 20 k PEO (25,000 Pa), approximately c^*, the polymer overlap concentration, the PEO is forced inside the lumen of the MTs, and the MTs convert to undistorted MTs in hexagonal bundles. At 18% 20 k PEO (400,000 Pa), all the MTs are in the hexagonal bundle phase.

understood (22). The centers of the macromolecules are excluded from a region around each particle because they cannot interpenetrate. If these 'excluded volumes' around the particles overlap, then the volume available to the macromolecules increases and the total entropy increases, which results in an effective attraction between the particles. This 'depletion attraction' can lead rod-like particles to form a variety of phases (23,24). DNA (25), actin (26), and MTs (27) have all been observed to form bundles in the presence of inert macromolecules. It has been proposed that these excluded volume effects help organize the cytoplasm (28).

The depletion attraction can be used as a powerful probe of intermolecular interactions. If the induced attraction causes the macromolecules to phase separate from the rod-like particles, then the interaction between rod-like particles can be measured using the ''osmotic stress'' technique (29). In this method a known osmotic pressure is applied by controlling the concentration of inert macromolecule, and the resulting spacing between particles is determined by x-ray scattering. The osmotic stress technique has been used to study a wide variety of systems; for example, the forces between viruses (30) have been measured and the interactions between DNA molecules have been extensively studied (31).

Unlike actin, DNA, and many other rod-like biological polyelectrolytes, MTs are hollow, which leads to additional possible effects of applied osmotic pressure. If the added inert macromolecule is large enough to be excluded from the MT lumen, then a pressure imbalance is created between the inside and outside of the MT. For a large enough pressure difference, the MTs buckle in a manner analogous to the buckling of a hollow tube with closed ends subjected to enormous hydrostatic pressure, such as a submarine in deep sea (27). The deformation of hollow tubes under pressure has been extensively studied but, to the best of our knowledge, this work is the first unambiguous determination of the structure of bundles of hollow tubes under radial pressure.

For deformable objects such as MTs, there is a connection between the osmotic pressure-induced buckling and the bundling caused by excluded volume effects. The strength of the depletion attraction is highly dependent on the shape of the attracting particles (32,33). The induced attraction between flattened particles, such as distorted MTs, can be orders of magnitude greater than between rounded particles, such as undistorted MTs. Thus increasing the osmotic pressure causes the MTs to buckle, and upon buckling the depletion attraction between MTs greatly increases so the buckled MTs form bundles (27).

The deformation of tubes under pressure can be used to measure the mechanical properties of the tubes. Previous mechanical measurements of MTs have been performed by a number of groups using various methods. The axial bending rigidity of MTs has been measured by observing the thermal fluctuations of filaments (34–37) and by manipulation with optical tweezers or hydrodynamic flow (34,37–39). Atomic force microscopy (AFM) has been used to probe the radial mechanical properties of MTs (40,41). Image analysis of cryoelectron micrographs has been used to analyze how MTs respond to internal stresses (42–45). Knowledge of the mechanics of MTs is important for understanding their behaviors and functions in vivo. In addition, MT mechanics can be used to gain insight into the molecular and mesoscopic interactions that underlie MT dynamic instability (36,42,44). Our work expands on these earlier measurements by describing new features of the radial mechanical properties of MTs that can be used to probe the interprotofilament interactions. The osmotic stress-small angle x-ray diffraction (SAXRD) method described here allows the microscopic mode of action of MT stabilizing agents to be directly investigated using mechanical perturbations.

We have subjected MTs to osmotic stress by mixing them with poly-(ethylene-oxide) (PEO), dextran, and bovine serum albumin (BSA). PEO and polymeric sugars induce attractive interactions between proteins by excluded volume effects (46,47). Indeed, it has previously been demonstrated that the interaction between PEO and tubulin is purely unfavorable (48). PEO and dextran do enhance MT polymerization (49), presumably through a depletion attraction mechanism, in a manner similar to the stabilizing effects of osmolytes on actin (50).

We have characterized MTs under osmotic stress on length scales from millimeters to nanometers using polarized microscopy, video-enhanced differential interference contrast (DIC) microscopy, fluorescence microscopy, whole mount and plastic-embedded thin section electron microscopy, and synchrotron and rotating-anode SAXRD. Our results are summarized in Fig. 1. With no or low concentration of added osmolytes, the added polymers have no effect on the MTs, but the MTs align due to steric interactions with each other. When the concentration of stressing polymer is increased, the MTs form bundles. If the polymers do not enter the MT lumen, then at high enough concentration, the MTs buckle to a noncircular cross section and pack into a lattice with rectangular symmetry. The MTs continue to distort as the osmotic pressure increases. This buckling and distortion is reversible. If the polymer can enter the MT, because of its small size or at high concentrations of medium size polymer, then hexagonal bundles of undistorted MTs are formed. We have used the osmotic stress technique in the hexagonal bundle phase to measure the interactions between MTs. The transition to the rectangular bundle phase and the associated MT deformations provide information on the mechanical properties of MTs, which in turn give insight into how taxol and MAPs stabilize MTs. The work presented in this manuscript is an elaboration and continuation of a previous short article (27).

MATERIALS AND METHODS

Materials

Tubulin and MTP were purified from bovine brains as described previously (8). MTP was obtained from three cycles of polymerization/depolymerization, and tubulin was purified from MTP by phosphocellulose chromatography. MTs were polymerized from tubulin at ~4 mg/ml in 50 mM PIPES (pH 6.8, adjusted with 80 mM NaOH), 1 mM $MgCl_2$, 1 mM EGTA, 1 mM guanine triphosphate (GTP), and 5% glycerol by incubating in a 37°C water bath for 20 min. Unless otherwise noted, MTs were stabilized by the addition of 20 μM taxol. Samples were made by diluting MTs 1:1 with PEO (Fluka, Seelze, Germany) solutions, so final buffer and taxol concentrations were half those listed above. Fluorescently labeled PEO was synthesized from mPEG20000-NH_2 (Shearwater, Huntsville, AL) and Lissamine rhodamine B sulfonylchloride (Fluka) in dichloromethane with triethylamine (Fluka) and purified by flash chromatography on a silica gel. The osmotic pressure exerted by solutions of 20 k PEO was obtained from a publicly available database (http://www.brocku.ca/researchers/peter_rand/osmotic/osfile.html #data, see Supplementary Methods for further information).

X-ray scattering

Synchrotron SAXRD experiments were performed at beamline 4-2 of the Stanford Synchrotron Radiation Laboratory during four runs, over the course of a year, using tubulin purified from four different preps. X-ray scattering patterns were reproducible throughout, including over the volume of a sample and between different samples from different preps on different runs. The scattering was done at 8.98 keV with a beam size of 0.2 × 0.2 mm and sample-to-detector distances of 2.2015 m, 2.1579 m, 2.2022 m, and 2.1660 m, determined using silver behenate as a standard. A charge-coupled device-based area detector (MarCCD165, Mar USA, Evanston, IL) was used. Scans were performed for an average of 12 min, over which time no sample damage occurred, which was explicitly checked for by performing multiple short scans. In-house experiments were performed on a custom-built rotating anode SAXRD set-up. Rotating anode scans were typically performed for 12 h and have lower resolution and lower signal/noise than synchrotron scans but display the same features.

The samples showed powder scattering, so images were averaged over 360° to obtain plots of scattering intensity versus momentum transfer, $q \equiv 4\pi/\lambda \sin\theta$. Where λ is the x-ray's wavelength and 2θ is the angle between the transmitted and scattered beams. All x-ray scans are raw data with no processing of any kind.

X-ray samples were centrifuged at 16,000 g for 1 h, transferred to 1.5 mm quartz capillaries, and left to sit at least 3 days before measurements were taken to ensure that the equilibrium osmotic stress was reached. Qualitatively similar data were obtained when SAXRD scans were taken immediately after samples were prepared. MTs are stable for days with sufficient taxol (10). To prevent MT depolymerization, measurements were taken immediately on samples with low concentrations of taxol.

Optical microscopy

A Nikon Diaphot 300 microscope with a Sutter Instrument (Novato, CA) Lambda LS xenon arc; an oil condenser; an oil, 1.4 numerical aperture, 60× objective with an additional 4× eye piece; and a Dage-MTI (Michigan City, IN) VE 1000 camera were used for high resolution video-enhanced DIC. Background subtraction, image enhancement, and two-frame averaging were performed with a Dage-MTI DSP-2000. Fluorescence images, and the corresponding DIC images, were taken with a Cooke (Romulus, MI) Sensicam QE monochrome digital camera, on the microscope described above, without the 4× eyepiece or image processing. Fluorescence images were high-pass filtered, Gaussian blurred, and contrast-adjusted with Adobe Photoshop. Coverslips and slides were cleaned with soap, ethanol, and water and sealed with wax.

Polarized microscopy images were taken with a Nikon Optiphot2-Pol microscope with a 5× objective and a Nikon Coolpix 990 camera; 3 mm × 0.3 mm rectangular capillaries were used.

Electron microscopy

Transmission electron microscopy experiments were performed at 80 kV. Whole mount samples were transferred to carbon-coated grids and stained with uranyl acetate. Samples for thin sections were centrifuged at 16,000 g for 1 h to form a pellet. Pellets were fixed with 2% glutaraldehyde (GA) and 0.2% tannic acid overnight, postfixed with 0.75% (w/v) OsO_4 for 1 h, stained en bloc with 1% uranyl acetate for 1 h, dehydrated with acetone, embedded in spur plastic, and cut to ~70 nm.

Modeling

For all calculations that treated MTs as homogeneous, isotropic, hollow cylinders, the MTs were taken to have an outer radius of 12.7 nm and an inner radius of 8.7 nm (2). Changing these values within physically reasonable limits does not qualitatively change the results. The surface charge of MTs at pH 6.8 was taken to be -0.87 e/nm^2 (calculated from the primary structure of tubulin with 2 bound Mg^{2+} ions, one molecule GTP, and one molecule GDP per dimer), and the salt concentration was 40 mM Na^+ and 0.5 mM $MgCl_2$ (as in our buffer).

RESULTS

PEO bundles MTs

MTs at high concentration are oriented on the micron and millimeter length scales (Fig. 2, *A* and *C*). It is not clear if the

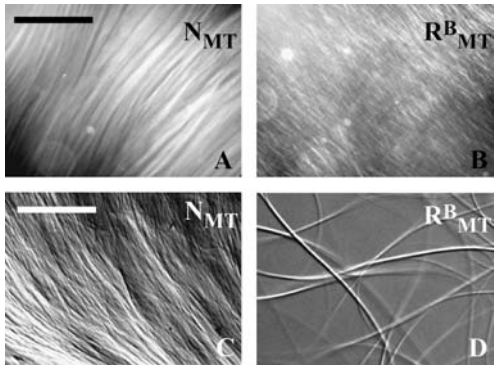

FIGURE 2 Optical micrographs of MTs and MT bundles with 20 k PEO. Polarized microscopy of (*A*) MTs with no added PEO and (*B*) MTs with 0.42% (wt/wt) 20 k PEO (scale bar = 500 μm). Video-enhanced DIC microscopy of (*C*) MTs with 0.2% 20 k PEO and of (*D*) MTs with 1% 20 k PEO (scale bar = 10 μm). With low concentration of added 20 k PEO (*A* and *C*), MTs are oriented on μm to mm length scales, denoted N_{MT}. MTs form bundles with higher concentrations of added PEO (*D*) which display weaker large-scale orientation (*B*). X-ray scattering experiments demonstrate that these bundles are in the rectangular phase, R^B_{MT}.

orientation is induced by flow, confinement, or the excluded volume interactions between MTs. It has been previously argued that MTs spontaneously align at comparable concentrations to form a true nematic liquid crystal (51), which is supported by a simple estimate of the volume fraction of rods necessary to form a nematic. Long rods of length L and radius R interacting through hardcore repulsion are predicted to form a nematic at a volume fraction of $\phi_N = (5.37\pi/4)(R/L)$ (52). Taking $R = 12.7$ nm and $L = 10$ μm, yields $\phi_N \approx 0.005$, comparable to the MT volume fraction used in this study. Therefore, we refer to the oriented MTs as being in the nematic phase.

For low concentrations of added 20 k PEO, the MTs remain nematic. The MTs begin to form bundles with >0.4% (w/w) 20 k PEO. On the millimeter length scale the bundles are less oriented than the nematic MTs (Fig. 2 *B*). The bundles are visible as thick fibers on the micron scale (Fig. 2 *D*). However, the resolution of optical images is ~250 nm, so other techniques are needed to probe the internal organization of the MT bundles.

Small angle x-ray scattering reveals the bundles' internal structure

We have performed a series of SAXRD experiments to study the nm scale structure of the MT bundles. The small angle scattering from solutions of MTs drastically changes as additional 20 k PEO is added (Fig. 3 *A*). For small concentrations of 20 k PEO the scattering is smoothly varying, but at higher concentrations multiple peaks are evident. These peaks shift, new peaks appear, and old peaks vanish as more 20 k PEO is added. All of these scattering data can be explained by the existence of three distinct structures: unbundled MTs, MT bundles with rectangular symmetry, and MT bundles with hexagonal symmetry.

For small concentrations of added 20 k PEO, the scattering is that of unbundled MTs, so only the MT form factor is seen (Fig. 3, *A* and *B*, N_{MT}). The scattering in the q range we examine probes structures on length scales ~6–60 nm and therefore does not contain information on the structure of the tubulin subunit, which is available at wider scattering angles (53). At small q, the MT's form factor is dominated by its diameter and wall thickness, and, for comparison, Fig. 3 *C* shows a model calculation of the scattering from a hollow cylinder of appropriate dimensions (Fig. 3 *C*, unbuckled). The minimum in the scattering data (Fig. 3 *B*, N_{MT}) are slightly filled in due to the presence of a small amount of tubulin which has not polymerized into MTs (54). If this background is properly accounted for, the hollow cylinder

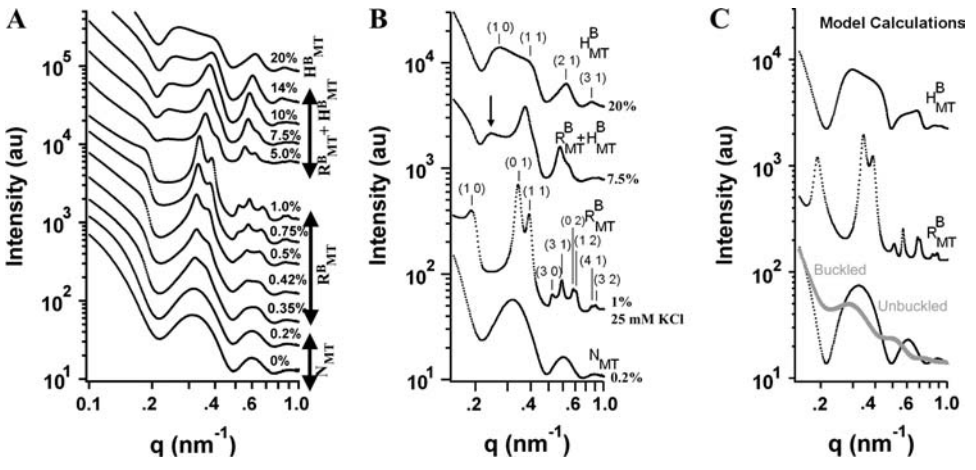

FIGURE 3 Small angle synchrotron x-ray diffraction scans of MTs with 20 k PEO. (*A*) The scattering patterns continuously evolve as the 20 k PEO concentration is increased from 0% (wt/wt) to 20%. All peaks, oscillations, and minima of the scattering can be accounted for by three structures: a nematic of single MTs (N^{MT}), bundles with rectangular symmetry (R^B_{MT}), and bundles with hexagonal symmetry (H^B_{MT}). (*B*) Up to nine peaks of the rectangular lattice and four peaks of the hexagonal lattice are visible, all of which can be indexed. The (1 0) rectangular peak is often difficult to discern but is more prominent with 25 mM added KCl (R^B_{MT}). Coexistence between bundles with rectangular and hexagonal symmetry is evident in many scans (R^B_{MT}+H^B_{MT}, *arrow* indicates hexagonal (1 0) peak. All other peaks are from rectangular bundles, indices not shown). (*C*) Model calculations of the scattering from isolated MTs (unbuckled), unbundled, distorted MTs (buckled), bundles of distorted MTs with rectangular symmetry (R^B_{MT}), and bundles of undeformed MTs with hexagonal symmetry (H^B_{MT}). See text for modeling details.

model (Fig. 3 *C*, unbuckled) can quantitatively describe the scattering from MTs in this q range (55). SAXRD is a sensitive measure of the average number of protofilaments in MTs (53). The measured form factors indicate that these MTs have an average of ~13 protofilaments, determined by comparing these SAXRD data with results from Andreu (53). An average of 13 protofilaments is expected for MTs stabilized by taxol after polymerization (10), as MTs in this study were.

SAXRD experiments measure the Fourier transform of the electron density of objects in the sample (56). The electron density of an MT bundle is a convolution of the electron density of a single MT with the two-dimensional lattice of delta-functions that define the arrangement of MTs in the bundle. Therefore the scattering of an MT bundle is the multiplication of the MT form factor, the Fourier transform of the electron density of a single MT, with the bundle structure factor, the Fourier transform of the two-dimensional lattice (56). Thus the scattering consists of Bragg peaks, determined by the structure factor, and the peak heights are modified by the smoothly varying form factor. The height and shape of peaks in the structure factor are determined by lattice vibrations, defects, finite-size effects, and other distortions, whereas the peak positions determine the symmetry and dimensions of the lattice. There are only five lattice types in two dimensions (57), and indexing the Bragg peaks seen in the bundle phases allows the lattice type and the associated lattice constants to be uniquely determined. With high concentration of 20 k PEO (Fig. 3, *A* and *B*, H^{B}_{MT}), the four peaks index to a hexagonal lattice with lattice constant $a_H = 4\pi/\sqrt{3}q_{10} = 26.97 \pm 0.2$ nm. Thus the MTs form hexagonally packed bundles with high amounts of added 20 k PEO (Fig. 1, 400,000 Pa). Fig. 3 *C*, H^{B}_{MT}, shows the calculated scattering from a hexagonal array of hollow cylinders with $a_H = 27$ nm. The structure factor peaks were taken to be Lorentzians with widths of 0.04 nm^{-1}, and separate amplitudes for each peak were chosen to mimic the data (Fig. 3 *B*, H^{B}_{MT}).

With moderate concentrations of 20 k PEO, the Bragg peaks index to a rectangular lattice (Fig. 3 *B*, R^{B}_{MT}). Surprisingly, these nine orders of diffraction peaks indicate that one of the lattice parameters, a_R, is smaller than the unperturbed MT diameter of 25.4 nm, whereas the other lattice parameter, b_R, is larger (Fig. 3 *B*, $R^{B}_{MT,}$ $a_R = 2\pi/q_{01} = 18.47 \pm 0.2$ nm and $b_R = 2\pi/q_{10} = 33.40 \pm 0.9$ nm; see Fig. 1 for illustrations of a_R and b_R). The only way that MTs can fit into this lattice structure is if the high pressure causes their shape to become distorted (Fig. 1). The bundles themselves are highly asymmetric. The bundle size, L_i, along a direction i, can be measured with Warren's approximation, in which the scattering close to a reciprocal lattice vector, G, results in a structure factor $\propto \exp(-|q - G|^2 L_i^2/4\pi)$. This yields a domain size of $L_{(1\ 0)} = 166$ nm along the (1 0) plane and a $L_{(0\ 1)} = 204$ nm along the (1 0) plane, so these bundles are ~5 MTs by 11 MTs, with more MTs along the axis that is more compressed. A model scattering curve for a rectangular lattice of ellipses with $a_R = 18.47$ and $b_R = 33.40$ nm is shown in Fig. 3 *C* (R^{B}_{MT}). In this model Lorentzian-shaped peaks were used with separate amplitudes for each peak, a width of 0.013 nm^{-1} in the (1 0) direction, and a width of 0.009 nm^{-1} in the (0 1) direction.

At intermediate concentrations of 20 k PEO, a coexistence of rectangular bundles and hexagonal bundles are observed (Fig. 3 *C*, $R^{B}_{MT} + H^{B}_{MT}$). All of the peaks in the scattering data (Fig. 3 *A*) can be indexed to rectangular or hexagonal lattice structures, with lattice parameters varying as the PEO concentration varies.

Although the MTs in the rectangular bundle phase are distorted, SAXRD measurements show that the MTs in the nematic phase remain undistorted for all PEO concentrations and under all conditions investigated. Fig. 3 *C* compares the expected scattering from an MT with a circular cross section (unbuckled) with the calculated scattering from an MT with an elliptical cross section (buckled). The dimensions of the model-deformed MTs, with a semiminor axis of 7.2 nm and a semimajor axis of 13.8 nm to the center of the MT wall, are those of the least deformed MTs in the rectangular bundle phase. The model curves of the buckled and unbuckled MTs are quite different. Most notably, the second and third maxima of the buckled MT form factor occur at q values similar to minima in the unbuckled MT form factor. Thus, SAXRD can easily distinguish between buckled and unbuckled MTs in the nematic phase, and only unbuckled MTs have been observed. For example, the form factor of MTs with no added 20 k PEO (Fig. 3 *A*, 0%) is nearly identical to the form factor of MTs directly before the transition to rectangular bundles (Fig. 3 *A*, 0.2%). There may be some conditions, which we have not yet examined, in which MTs are buckled in the nematic phase.

The transition to the rectangular bundle phase is reversible

The transition from unbundled, nematic MTs to bundled MTs in the rectangular phase with increasing 20 k PEO can be reversed by decreasing the concentration of 20 k PEO. Fig. 4 *A* (1%) shows SAXRD results from MTs with 1% 20 k PEO in the rectangular bundle phase. When these MTs are centrifuged to a pellet and resuspended in buffer such that the final 20 k PEO concentration has been reduced to 0.2%, SAXRD scans show that the MTs return to unbundled, undamaged MTs (Fig. 4 *A*, 20 k PEO reduced to 0.2%). Furthermore, this SAXRD scan demonstrates that the number of protofilaments per MT remains unchanged before and after being in the rectangular bundle phase. Whole mount electron microscopy confirms that MTs previously in the rectangular bundle phase are intact and undamaged (Fig. 4 *A*, *inset*).

The transition to the rectangular bundle phase is also reversible by the addition of GA. In-house SAXRD scans show that MTs in the rectangular bundle phase become less

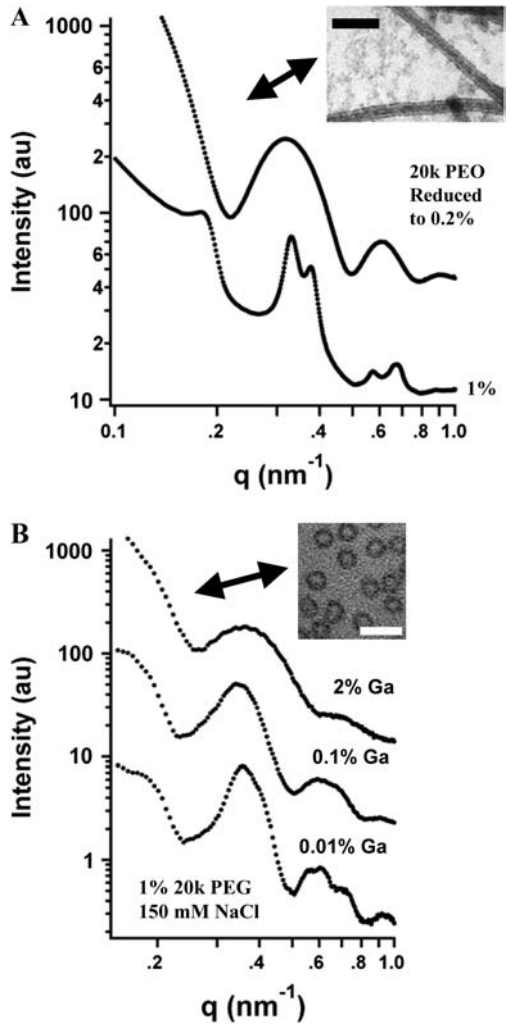

FIGURE 4 The transition to rectangular bundles is reversible. (*A*) Small angle synchrotron x-ray diffraction scans of MTs with 1% (wt/wt) 20 k PEO show bundles with rectangular symmetry. If these MTs are spun into a pellet, the supernatant is removed and the MTs are resuspended in solution with 0.2% 20 k PEO, the solution reconverts to a nematic of undistorted, undamaged MT (*A*), as seen by the SAXRD scan showing form factor scattering and (*A*, *inset*, scale bar = 50 nm) confirmed by whole mount electron microscopy. (*B*) Small angle rotating anode x-ray scans of MTs, with lower resolution and greater noise, demonstrate that MTs that were buckled 1% 20 k PEG and 150 mM NaCl, unbuckle with the addition of 2% GA. Plastic embedded electron microscopy cross sections confirm that previously buckled MTs reconvert to undistorted, unbundled MTs (*B*, *inset*, scale bar = 50 nm).

distorted if GA is added to the preformed bundles (Fig. 4 *B*), where the (0 1) peak is seen to move to smaller q, indicating an increase in a_R, as the concentration of GA increases from 0.01% to 0.1%. If the concentration of added GA is high enough, the MTs become unbundled and unbuckled (Fig. 4 *B*, 2% GA). Electron microscopy of plastic embedded cross sections of MTs that were formerly in the bundled phase confirms that GA causes these MTs to unbundle and revert to undistorted MTs (Fig. 4 *B*, *inset*).

The rectangular bundle phase forms in the presence of polymers that are excluded from the MT lumen

The nature of the formed bundle phase depends on the method or substance used to exert osmotic pressure, as summarized in Table 1. The rectangular bundle phase forms when MTs are mixed with BSA. For low concentrations of added BSA the MTs form a nematic, whereas at higher concentrations the rectangular bundle phase is observed. The hexagonal bundle phase is never seen even with up to 20% BSA in solution. BSA is a negatively charged globular protein ~9 nm × 4 nm × 8 nm (58), with a radius of gyration (R_g) of 3.2 nm (59). Thus BSA is expected to be too large to appreciably enter the MT lumen. If BSA is modeled as a capsule of appropriate dimensions, then only ~2% is expected to partition into the MTs (60).

Rectangular bundles are also observed with added 500 kd dextran and 100 k PEO. Approximating 500 kd dextran and 100 k PEO as ideal polymers, both with $R_g \sim 18$ nm (61,62), essentially all of the added polymer should be excluded from the MT interior (63). Only unbundled MTs in the nematic phase and bundles in the rectangular phase are seen with 500 kd dextran, up to 8%, and 100 k PEO, up to 5%, the hexagonal bundle phase is never observed. In contrast, only unbundled MTs and hexagonal bundles are observed with added 600 PEO, bundles in the rectangular phase are never seen. 600 PEO is a small polymer, $R_g \sim 1$ nm (61), and at least ~75% of the added polymer is predicted to enter the MT lumen (63).

Furthermore, the polymer does not need to be in physical contact with the MTs to convert them to the rectangular bundle phase. If the MTs are incubated against a solution of 20 k PEO, with the two solutions separated by a semipermeable membrane, the rectangular bundle phase still forms; however, the hexagonal bundle phase is not observed. In these experiments, buffer is drawn across the semipermeable membrane, increasing the concentration of MTs until the mechanical pressure exerted by the MTs equals the osmotic pressure of the 20 k PEO. The transition from nematic, unbundled MTs to rectangular bundles occurs at a similar concentration of added 20 k PEO independent of whether the polymer is separated by a semipermeable membrane or directly mixed with the MTs. Less than 2% of added 20 k PEO, with $R_g \sim 7$ nm (61), should partition into the MT

TABLE 1 Summary of bundle phases present (+) or absent (−) with different means of producing osmotic pressure

	R^B_{MT}	H^B_{MT}
100 k PEO	+	−
20 k PEO	+	+
0.6 k PEO	−	+
BSA	+	−
500 kd dextran	+	−
Semipermeable membrane (20 k PEO)	+	−

interior for low concentrations of added polymer (63) even when the polymer is in contact with the MTs.

The connection between formation of the rectangular bundle phase and exclusion of stressing polymer from the MT lumen is further supported by optical microscopy measurements. Rectangular bundles created with fluorescent 500 kd dextran (Fig. 5, 8% 500 k dextran) or small amounts of fluorescently labeled 20 k PEO (Fig. 5, 1% 20 k PEO) appear dark in fluorescence. This proves that the dextran and 20 k PEO tend to be excluded from the rectangular bundle phase. In contrast, if the concentration of unlabeled 20 k PEO is increased, keeping the concentration of fluorescently labeled 20 k PEO constant so the bundles are in the hexagonal phase, then these bundles are not different from background in fluorescence images (Fig. 5, 20% 20 k PEO). This is consistent with 20 k PEO entering MTs when they convert to hexagonal bundles. The entry of polymer into MTs at high concentration is expected from theory (64), which predicts that the ease with which polymers enter a confining tube, such as an MT, greatly increases as the polymers begin to overlap and exert forces on each other. Consistent with this, the hexagonal bundles appear at a concentration of added 20 k PEO near their overlap concentration of $c^* \sim 7.5\%$ (w/w). Thus, if the stressing polymers are excluded from the MT lumen, then the pressure difference across the MT wall causes the MTs to buckle to a noncircular cross section. These buckled MTs form rectangular bundles due to depletion attraction. If the polymer can enter the MTs, either because the polymer is small or is forced in at high concentration, then the MTs are not distorted. Depletion attraction causes undistorted MTs to aggregate into hexagonal bundles at high enough concentrations of added polymer.

Solution conditions strongly affect MT bundling

The bundling of MTs, particularly the osmotic pressure required to form the rectangular bundle phase, is strongly affected by solution conditions. The presence of MAPs greatly influences MT bundling (Fig. 6). MAPs were introduced by polymerizing MTs from mixtures of purified tubulin and MTP, which is partially purified tubulin that is ~30% MAP and ~70% tubulin by weight (65). The presences of very small amounts of MAPs greatly suppress the nematic to rectangular bundle transition. MTs polymerized with 5% MTP and 95% tubulin contain only ~1.5% MAPs by weight, but this substantially increases the concentrations of stressing 20 k PEO needed to induce the transition to rectangular bundles (compare Fig. 6 *A* and Fig. 3 *A*). MTs with ~15% MAPs (50% MTP) do not display the rectangular bundle phase at any osmotic pressure, though the hexagonal bundle phase is still present with high concentrations of added 20 k PEO (Fig. 6 *B*). No rectangular bundles are observed with 100% MTP, with no taxol, at physiological ionic strength (Fig. 6 *C*). The osmotic pressure-%MTP phase diagram with 20 k PEO is shown in Fig. 7. As noted above, the most significant change with increasing MAPs is a large increase in the osmotic pressure required to induce rectangular bundles, and with enough MAPs no rectangular bundles are present.

The transition from nematic, unbundled MTs to the rectangular phase of MT bundles is also affected by the ionic strength of the solution. Increasing the amount of added KCl in solution reduces the concentration of 20 k PEO required to induce rectangular bundles (compare Fig. 8 *A* and Fig. 8 *B*). These data are summarized in Fig. 9 *A*, where the osmotic pressure required to induce rectangular bundles with 20 k PEO is plotted as a function of added KCl.

In contrast to the effects of MAPs, which increase the pressure required to induce rectangular bundles, and KCl, which decreases the pressure required to form rectangular bundles, the presence of the chemotherapy drug taxol has no effect on the nematic to rectangular bundle phase boundary in MTs (Fig. 9 *B*). In the range of taxol concentrations investigated, tubulin polymerization is greatly enhanced (8) and the stoichiometry of bound taxol to tubulin dimers in MTs varies from ~0.2 to ~0.8 (calculated using the known binding constant of taxol (66)). It is surprising that taxol and MAPs have such different effects on the transition to the rectangular bundle phase, as both stabilize MTs against depolymerization.

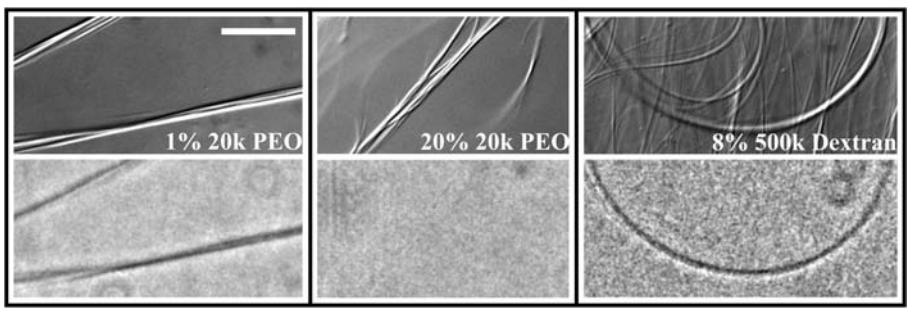

FIGURE 5 Osmotic stressing polymers do not enter the MT lumen in the rectangular but do enter the MT lumen in the hexagonal phase. DIC microscopy, upper, and corresponding fluorescence microscopy, lower, of MTs with 1% 20 k PEO, 20% 20 k PEO, and 8% 500 kd dextran (scale bar = 10 μm). All samples contain 100 mM monovalent salt. Both PEO samples have 0.1% fluorescently labeled 20 k PEO. All of the dextran is fluorescently labeled. The bundles with 1% 20 k PEO and 8% 500 kd dextran, which x-ray indicates are rectangular, are dark in fluorescence showing that the stressing polymers are excluded from these bundles. The fluorescence images are uniform with 20% 20 k PEO, which are hexagonal, and this is consistent with PEO entering these bundles.

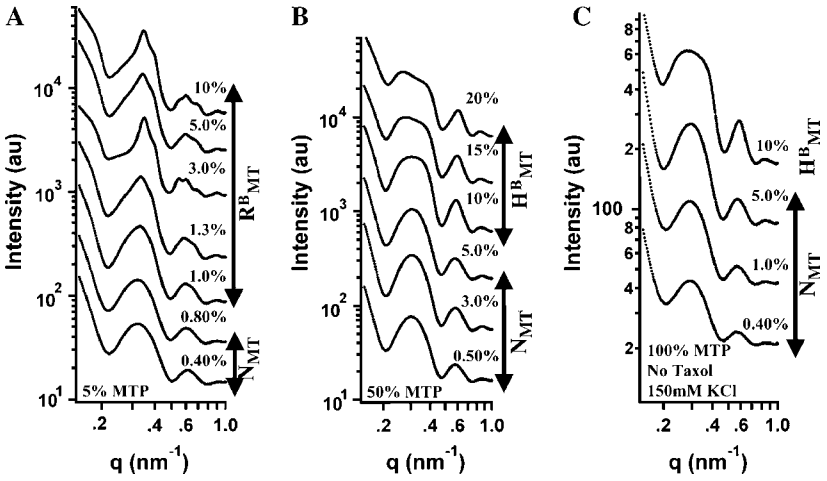

FIGURE 6 Small angle synchrotron x-ray diffraction scans of 20 k PEO with MTs, polymerized in the presence of partially purified MTP, which is ~30% MT-associated protein and ~70% tubulin. (*A*) MTs polymerized with 5% MTP form rectangular bundles but only with higher concentrations of 20 k PEO. (*B*) With 50% MTP hexagonal bundles are present for high 20 k PEO concentrations and rectangular bundles are not observed. (*C*) 100% MTP with no taxol and 150 mM KCl also display no rectangular bundles.

In the rectangular bundle phase, MTs continue to distort as the osmotic pressure increases

The MTs become increasingly distorted with increasing osmotic pressure. a_R decreases linearly with the logarithm of the pressure, with the same slope for MTs with MAPs (Fig. 10 *A*), MTs with added KCl (Fig. 10 *B*), and MTs with various concentrations of added taxol (Fig. 10 *C*). The continued deformation of MTs beyond the initial buckling most likely provides additional information on the mechanics of the MT walls. We cannot rigorously rule out the possibility that the dependence of a_R on osmotic pressure is controlled by the interactions between MT walls, but the independence of the postbuckling behavior on solution conditions makes this interpretation unlikely.

The scatter in b_R is much greater than the scatter in a_R because the (1 0) is often not directly observed in SAXRD experiments (see Fig. 3), so the value of b_R must be calculated from the positions of higher order peaks. b_R is constant or slightly increases with increasing pressure (Fig. 10 *D*). The perimeter of the distorted MTs can be calculated from the knowledge of a_R and b_R. The perimeter is plotted as a function of osmotic pressure in Fig. 10 *E*, assuming the MTs have an elliptical cross section and there is 2 nm of water between MTs in the bundle. The calculated perimeter of the distorted MTs differs from the perimeter of an undistorted MT by <20%. Because the MT dimensions are much larger than any reasonable water spacing, changing the water spacing does not significantly affect the calculated MT perimeter.

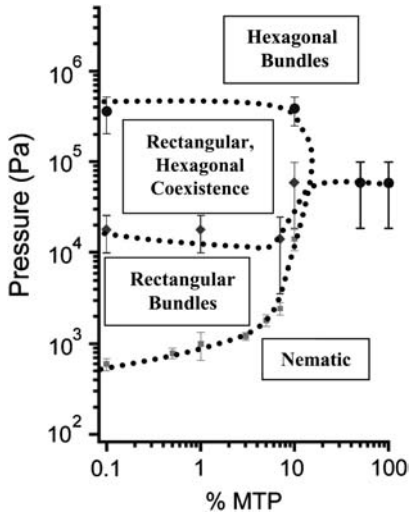

FIGURE 7 Osmotic pressure-MTP phase diagram measured with 20 k PEO. Tubulin (phosphocellulose chromatography purified) phase boundaries are indicated as 0.1% MTP. Dotted lines are guides to the eye. Regions where rectangular bundles are observed are shaded with a grid. Increasing the percentage of MTP results in a drastic increase in the pressure required to observe rectangular bundles. No rectangular bundles are observed for >10% MTP.

In the hexagonal bundle phase, MT spacing decreases with increasing osmotic pressure

The center-to-center distance between MT in the hexagonal phase, a_H, illustrated in Fig. 1, decreases with increasing osmotic pressure. This trend is clear from following the

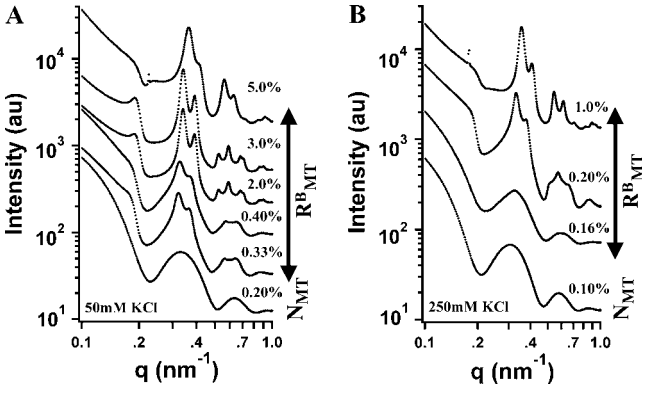

FIGURE 8 Small angle synchrotron x-ray diffraction scans of MTs with 20 k PEO in the presence of added (*A*) 25 mM KCl and (*B*) 250 mM KCl. Increasing KCl concentration drives the nematic to rectangular bundle transition to a lower concentration of 20 k PEO.

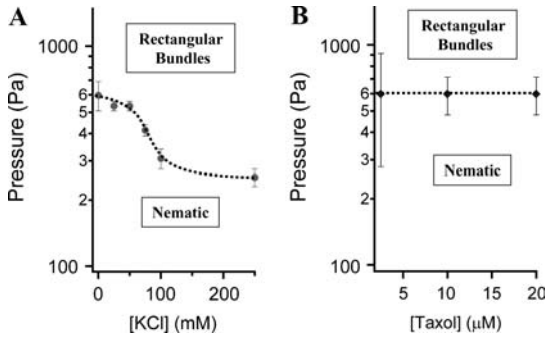

FIGURE 9 (*A*) Pressure-KCl and (*B*) pressure-taxol phase diagrams, near the nematic-rectangular bundle phase boundary, for MTs with 20 k PEO. Dotted lines are guides to eye. The pressure required to form rectangular bundles decreases with increasing KCl concentration but is unaffected by taxol concentration.

location of the (1 0) hexagonal peak in the raw x-ray data shown in Fig. 3 *A* (this peak is indexed in Fig. 3 *B*). The MT wall-to-wall distance is $D = a_H - 2R$, where R is the MT radius, and, since the MTs are in a hexagonal lattice, the force per unit length between them is $F = 2/\sqrt{3}R\pi_{osm}$, where π_{osm} is the applied osmotic pressure (31). a_H (and D) versus osmotic pressure (and F) is plotted in Fig. 11. These data measure the inter-MT interactions and are well fit by an exponential, $F = 72\,\text{pN/nm}\exp(-D/1.44\,\text{nm})$ (Fig. 11, *dashed line*). This measurement is in close agreement with the predicted force per unit length from Poisson-Boltzmann theory (67) for two charged cylinders with the appropriate radius, assuming constant surface potential: $F = 52\,\text{pN/nm}\exp(-D/1.47\,\text{nm})$. The surface potential was numerically calculated using the Graham equation from the MT surface charge. The slight discrepancy between the predicted and observed coefficient for the exponential may be caused by an increased repulsion from the localization of charge on the disordered, protruding C-terminus. MTs are highly negatively charged (68), so it is not surprising that the interaction between MTs is dominated by electrostatic double layer forces, as has also been measured for viruses (30) and DNA under appropriate conditions (69).

DISCUSSION

Implications for MT mechanics: P_{cr} measures interprotofilament interactions

The transition from unbundled, undistorted MTs to rectangular bundles of MTs with noncircular cross sections is due to the elastic instability of MTs under osmotic pressure. Thus the critical pressure required to buckle MTs, P_{cr}, provides a measure of their mechanical properties. We have determined $P_{cr} = 600 \pm 90$ Pa by measuring unbuckled nematic MTs at 510 Pa and buckled MTs in rectangular bundles at 690 Pa.

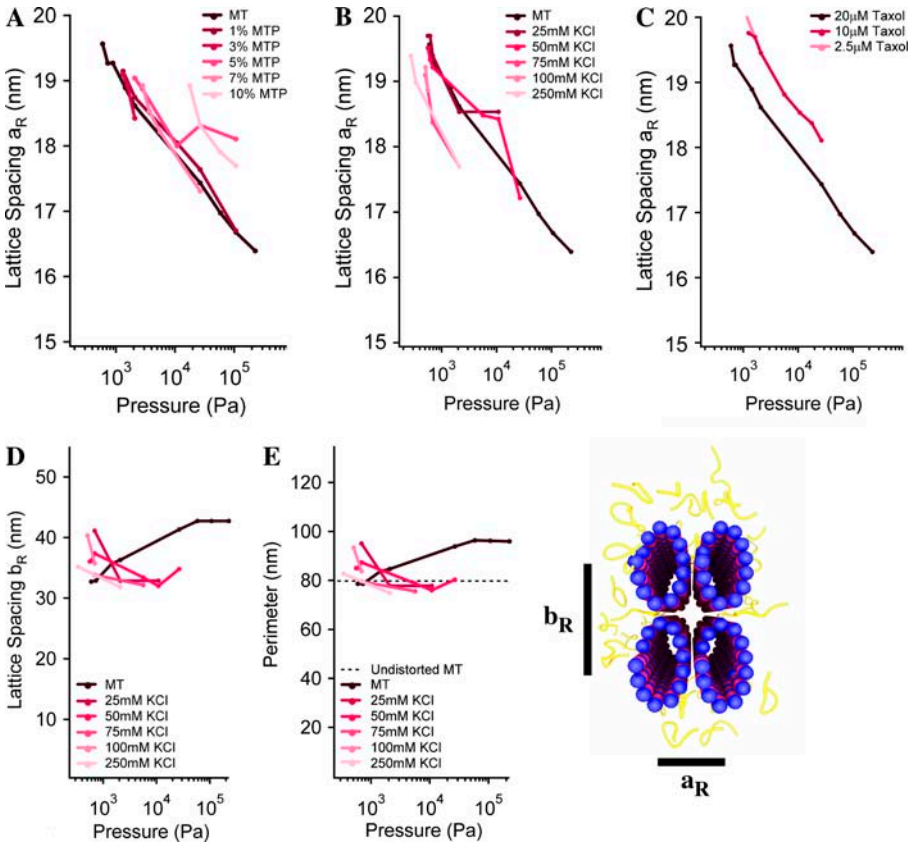

FIGURE 10 Continued deformation of rectangular bundles with increasing osmotic pressure, a_R and b_R, measured by small angle x-ray scattering are defined as in the cartoon. The slope of a_R versus the logarithm of pressure is the same for (*A*) all amounts of MTP, (*B*) all concentrations of KCl, and (*C*) all concentrations of taxol. (*D*) b_R and (*E*) the calculated MT perimeter versus osmotic pressure (see text).

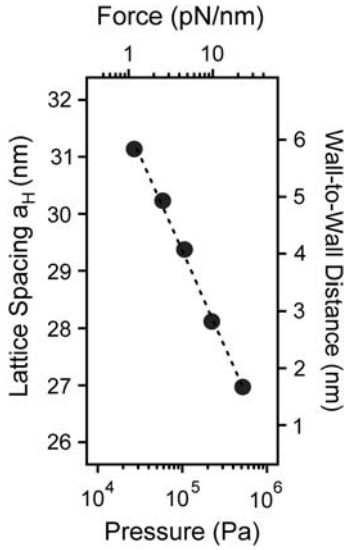

FIGURE 11 In the hexagonal bundle phase, the MT spacing decreases with increasing osmotic pressure. The measured lattice spacing a_R (*left*), the MT center-to-center distance, can be used to obtain the MT wall-to-wall distance (*right*). The applied osmotic pressure (*bottom*) can be used to calculate the force per unit length between MTs (*top*). See text for details. The dashed line is a best fit to the data.

If MTs are treated as homogeneous, isotropic, hollow cylinders, then MT bending measurements indicate a Young's modulus for tubulin of ~2 GPa, which is similar to other proteins (70). Using the same model of MTs as elastic hollow cylinders that explains the bending measurements, a buckling pressure of $P_{cr} = Eh^3/4(1-\nu^2)R^3 = 18.5$ MPa is predicted (71), where E is the Young's modulus of the MT wall, h is the MT wall thickness, and ν is the Poisson ratio for the material that makes up the MT wall (taken to be 0.4, similar to nylon). This calculated value of P_{cr} is over four orders of magnitude greater than our measured value. However, it is not surprising that the simple model described above fails because MTs are not homogeneous, isotropic objects. Large scale molecular level electrostatics calculations (72), simulations of course-grained mechanical properties (73), and simple models of dynamic instability (74) predict that the intermolecular interactions that connect protofilaments are much weaker than longitudinal tubulin bonds and the intramolecular interactions within a tubulin dimer. The derived value of the Young's modulus, along with cryoelectron microscopy measurements (43), argues that the resistance to axial bending is due to deformation of the tubulin subunit. This strongly suggests that low P_{cr} we measure is due to the weak compliance of the lateral bond between protofilaments.

An estimate of the lateral interaction between protofilaments may be obtained from P_{cr} by a standard linear elastic stability analysis (75) of a simple model of the MT. We treat the MT cross section as consisting of protofilaments of diameter $l \sim 5.0$ nm, connected by linear springs of spring constant k, which enforce the desired angle, θ_0, between the subunits. The protofilaments are considered to be incompressible at these low pressures because, assuming the protofilament can be treated as homogeneous, isotropic elastic solids with a Young's modulus of 2 GPa, which is typical for proteins (70), the expected relative change in dimensions is $<1\%$ at the buckling transition. Such a structure buckles at a critical pressure $P_{cr} \sim 0.81k/l^2$ (see Supplementary Material). For our measured buckling pressure of $P_{cr} = 600 \pm 90$ Pa this leads to a very small spring constant of $k \sim 4.4 \times 10^{-3} \pm 0.7 \times 10^{-3}\, k_bT/nm$, which implies that ~28 tubulin dimers, which is ~224 nm long, must stack to resist thermal fluctuations.

The continued deformation of MTs with increasing osmotic pressure provides additional information on the mechanical properties of MTs. The postbuckling compliance seems to have a different origin than the weak interprotofilament bonds that determine the initial buckling instability. The postbuckling behavior, unlike P_{cr}, is largely independent of solution conditions, and the initial deformation due to buckling requires less pressure than subsequent deformations of the same magnitude. For example, increasing the osmotic pressure from 300 Pa to 600 Pa causes the MTs to buckle from a circular cross section with a diameter of ~25 nm to a noncircular shape with a short dimension of ~19 nm, but further increasing the osmotic pressure to 200,000 Pa only decreases the short dimension to ~16 nm. We currently have no model with which to interpret the postbuckling behavior, but a very rough understanding of the source of compliance can be obtained by calculating an effective Young's modulus of the entire MT, $E_{MT} \approx \Delta PL/\Delta L \approx (200,000\,\text{Pa}) \times (19\,\text{nm})/(19\,\text{nm} - 16\,\text{nm}) = 1.3\,\text{GPa}$, where $\Delta L/L$ is the fractional change in length of the short dimension caused by the change in pressure, ΔP. This value of E_{MT} suggests that the resistance to postbuckling deformation, like the resistance to bending, is due to the distortion of the tubulin subunits, as opposed to the weak interprotofilament bond that is responsible for the initial buckling.

Our work is complementary to previous imaging and mechanical radial indentation studies of MTs with AFM (40,41,76), which enables the properties of individual MTs to be examined. The mechanical properties measured in the AFM experiments may be consistent with the stiff postbuckling behavior we observe with the osmotic stress-SAXRD technique. The AFM experiments did not observe an initial soft deformation, which may be due to the large minimum pressure exerted by the AFM tip or the MTs being deformed due to absorption to a surface, and measured MT heights by AFM are slightly smaller than expected, which is consistent with both these explanations (40,76). However, a quantitative comparison of results from AFM and osmotic stress-SAXRD is difficult because in the AFM experiments MTs are absorbed to a surface, the interaction between the surface and MTs and the AFM tip and MTs is poorly categorized, and the absolute height of the MTs is uncertain. It is currently unclear if MT-MT interactions are important

for interpreting the results of the osmotic stress-SAXRD technique. More detailed modeling of the mechanical properties of MTs is needed to synthesis the results from different experimental techniques.

Considerations on the structure of MT bundles

Whereas the MT buckling transition can be understood using simple models and the bundle formation occurs due to the depletion attraction, the reason that buckled MTs form bundles with rectangular internal symmetry is less clear. Some models of carbon nanotube bundles under pressure (77,78), and more abstract theories of stiff polymers with angular frustration (79), indicate that body-centered rectangular symmetry (perhaps with a herringbone structure) should be preferred. More recently, molecular dynamics simulations have shown that a face-centered oblique lattice of parallel carbon nanotubes buckled under pressure is more stable than the herringbone structure proposed in previous studies (80). Those authors did not compare the relative stability of those oblique lattices of parallel buckled tubes with the rectangular lattice of parallel buckled tubes found in our study. In addition, it is unclear why the overall shape of these MT bundles is asymmetric with more MTs along the more compressed axis, but it is interesting to note that depletion attraction between colloidal disks also leads to similarly asymmetric aggregates (33).

We have shown that osmotic stress can lead to the radial buckling of MTs. In theory, other types of elastic failures of MTs under osmotic stress are possible. At very high osmotic pressure, MTs might additionally fail via an axial local surface buckling (71) or an axial Euler buckling (71,75). It has previously been observed that MTs polymerizing against a barrier undergo an Euler buckling instability (81).

The hexagonal bundles form when the stressing polymer can enter the MT lumen. The entry of medium size polymer into MTs only at high concentration is consistent with theory (64), and similar effects have been seen with the partitioning of PEO in ion channels (82). Our measurements do not address the pathway by which the polymers enter MTs; they may enter through the open MT ends or through holes in the MT wall (2).

MT stabilization and interprotofilament interactions

We have provided strong evidence that P_{cr} provides a measure of the interprotofilament interactions and the osmotic stress-SAXRD technique is the first method that allows this to be probed. The interprotofilament bond is crucial for determining the dynamics of MT polymerization and depolymerization (5,74). The flexibility of the interprotofilament bond may also be important in MT nucleation and it may be responsible for variations in the number of protofilaments per MT.

MTs become destabilized in the presence of monovalent salt in excess of 100 mM (6), which corresponds to 60 mM added KCl in our experiments. P_{cr} decreases with added KCl in excess of this amount (Fig. 9 *A*), suggesting that the destabilization is due to weakening of the interprotofilament interactions. This is not surprising as observations from high resolution MT models (2), along with detailed computer simulations (72), suggest that the interprotofilament bonds are largely electrostatic in nature.

The addition of GA causes MTs in the rectangular bundle phase to become less distorted. If enough GA is added, these MTs unbuckle and revert to an unbundled state (Fig. 5 *B*). The unbundling of MTs is connected to their unbuckling, because when MTs revert to a rounded, undistorted shape the depletion attraction between then greatly decreases. These experiments demonstrate that GA increases the mechanical stiffness of MTs, including that due to compliance of the weak interprotofilament bound. The mechanical strengthening of MTs by GA has been previously measured by AFM (40).

MTs in neurons are much more stable than MTs in other cell types due to the action of MAPs (11,12). The presence of neuronal MAPs causes a dramatic increase in P_{cr}. MTs polymerized with 10% MTP are ~3% MAP and ~97% tubulin by weight, but the P_{cr} of such MTs is over 20 times greater than the P_{cr} of MTs polymerized from pure tubulin (Fig. 10). Thus the osmotic stress-SAXRD technique provides the first demonstration that MAPs increase interprotofilament interactions, presumably by directly cross-linking protofilaments, but this may also be due to a MAP-induced conformational change in tubulin.

Substoichiometric binding of the anticancer drug taxol enhances MT polymerization and inhibits depolymerization (8). Increasing taxol concentration from 2.5 μM to 20 μM has a large effect on MT polymerization, with the polymer mass at steady-state increasing by approximately a factor of two over this range of taxol concentrations (8). However, P_{cr} does not change, within error (approximately a factor of two), over this concentration range of taxol. In sharp contrast to the effects of taxol, increasing the concentration of MAPs from ~0.2% to ~3% (0.5% MTP to 10% MTP) has a more modest effect on MT stability, with polymer mass in steady state increasing by ~40%, as estimated from results with τ (11), but a much larger effect on P_{cr}, which increases nearly 20-fold. Thus, over the tested concentration ranges, taxol has a large effect on MT polymerization and a small effect on P_{cr}, whereas MAPs have a more modest effect on MT polymerization but a much larger effect on P_{cr}. Thus taxol does not stabilize MTs by increasing the interaction between protofilaments. These results support an earlier suggestion that taxol functions by preventing the straight-to-curved conformational change normally associated with GTP hydrolysis (10). Our work shows that taxol and the MAPs tested here stabilize MTs through different microscopic mechanisms.

CONCLUSION

We have presented measurements that provide information on the mechanical properties of MTs, the entry of substances into the MT lumen, and the nature of MT-MT interactions. By determining P_{cr} under various solution conditions, our work has provided the first estimate, to our knowledge, of the spring constant of the interprotofilament bond and given insight into the mechanism by which MAPs and taxol stabilize MTs. It will be interesting to apply this probe of the interprotofilament bond strength to other stabilizing agents, such as specific MAPs, other drugs, nonhydrolyzable GTP analogs, and destabilizing agents, such as Ca^{2+} and low temperatures. In addition, we plan on further investigating MT-MT interactions to discover how various MAPs alter these interactions. The continued elastic deformation of MTs with increasing osmotic pressures gives additional information on the radial mechanical properties of MTs and it will be profitable to combine this with an analysis that includes more sophisticated modeling of the MT wall.

Our work raises questions about the state of MTs inside the crowded environment found in cells. Cytoplasm is typically 20% protein by weight, and macromolecular crowding is believed to be significant at such high concentrations with important ramifications for cellular architecture and macromolecular interactions (28). The internal pressure of cells can be MPas (83), which is orders of magnitude greater than the osmotic pressure required to buckle MTs composed of pure tubulin. There seem to be three possibilities: MTs are sometimes buckled in vivo, one of the physiological roles of MAPs is to prevent MTs from buckling, or some of the osmotic stressing agents enter the MT lumen. Even if the rectangular phase of buckled MTs is suppressed inside cells, the osmotic pressure is still high enough to form hexagonal bundles through depletion attraction, and close packed hexagonal bundles of MTs have been observed in stressed cells (84).

More broadly, understanding dynamic instability of MTs, and the manner in which it is modified by distinct MAPs and drugs, is of fundamental biological and medical significance. The osmotic stress-SAXRD technique described in this work provides the first method, to our knowledge, for probing how various agents affect interprotofilament interactions. We hope that work on interactions, such as presented in this study, will be combined with structural models and MT polymerization measurements to develop a quantitative microscopic understanding of dynamic instability.

SUPPLEMENTARY MATERIAL

An online supplement to this article can be found by visiting BJ Online at http://www.biophysj.org.

We are grateful to Bob McMeeking and Robijn Bruinsma for insightful conversation. We thank Jenny Ross for assistance with experiments with dextran.

U. Raviv acknowledges the support of the International Human Frontier Science Program Organization. This work was supported by National Science Foundation grants DMR 0503347, CTS 0404444, and CTS 0103516, National Institutes of Health grants GM-59288 and NS-13560, and Department of Energy contract No. W-7405-ENG-36 with the University of California. The Materials Research Science and Engineering Center at the University of California, Santa Barbara, is supported by National Science Foundation DMR-0080034. The Stanford Synchrotron Radiation Laboratory is supported by the Department of Energy.

REFERENCES

1. Lowe, J., H. Li, K. H. Downing, and E. Nogales. 2001. Refined structure of alpha beta-tubulin at 3.5 Å resolution. *J. Mol. Biol.* 313:1045–1057.
2. Li, H., D. J. DeRosier, W. V. Nicholson, E. Nogales, and K. H. Downing. 2002. Microtubule structure at 8 Å resolution. *Structure.* 10:1317–1328.
3. Chretien, D., S. D. Fuller, and E. Karsenti. 1995. Structure of growing microtubule ends: two-dimensional sheets close into tubes at variable rates. *J. Cell Biol.* 129:1311–1328.
4. Mandelkow, E. M., E. Mandelkow, and R. A. Milligan. 1991. Microtubule dynamics and microtubule caps: a time-resolved cryo-electron microscopy study. *J. Cell Biol.* 114:977–991.
5. Desai, A., and T. J. Mitchison. 1997. Microtubule polymerization dynamics. *Annu. Rev. Cell Dev. Biol.* 13:83–117.
6. Olmsted, J. B., and G. G. Borisy. 1975. Ionic and nucleotide requirements for microtubule polymerization in vitro. *Biochemistry.* 14: 2996–3005.
7. Jordan, M. A., and L. Wilson. 2004. Microtubules as a target for anticancer drugs. *Nat. Rev. Cancer.* 4:253–265.
8. Derry, W. B., L. Wilson, and M. A. Jordan. 1995. Substoichiometric binding of taxol suppresses microtubule dynamics. *Biochemistry.* 34: 2203–2211.
9. Amos, L. A., and J. Lowe. 1999. How taxol stabilises microtubule structure. *Chem. Biol.* 6:R65–R69.
10. Arnal, I., and R. H. Wade. 1995. How does taxol stabilize microtubules? *Curr. Biol.* 5:900–908.
11. Panda, D., B. L. Goode, S. C. Feinstein, and L. Wilson. 1995. Kinetic stabilization of microtubule dynamics at steady state by tau and microtubule-binding domains of tau. *Biochemistry.* 34:11117–11127.
12. Bunker, J. M., L. Wilson, M. A. Jordan, and S. C. Feinstein. 2004. Modulation of microtubule dynamics by tau in living cells: implications for development and neurodegeneration. *Mol. Biol. Cell.* 15: 2720–2728.
13. Lee, V. M. Y., M. Goedert, and J. Q. Trojanowski. 2001. Neurodegenerative taupathies. *Annu. Rev. Neurosci.* 24:1121–1159.
14. Cassimeris, L., and C. Spittle. 2001. Regulation of microtubule-associated proteins. *Int. Rev. Cytol.* 210:163–226.
15. Hirokawa, N. 1991. Molecular architecture and dynamics of the neuronal cytoskeleton. *In* The Neuronal Cytoskeleton. R. D. Burgoyne, editor. Wiley-Liss, New York. 5–74.
16. MacRae, T. H. 1992. Microtubule organization by cross-linking and bundling proteins. *Biochim. Biophys. Acta.* 1160:145–155.
17. Lida, J., T. J. Itoh, H. Hotani, K. Nishiyama, H. Murofushi, J. C. Bulinski, and S. Hisanaga. 2002. The projection domain of MAP4 suppresses the microtubule-bundling activity of the microtubule-binding domain. *J. Mol. Biol.* 320:97–106.
18. Chen, J., Y. Kanai, N. J. Cowan, and N. Hirokawa. 1992. Projection domains of MAP2 and tau determine spacings between microtubules in dendrites and axons. *Nature.* 360:674–677.
19. Chapin, S. J., J. C. Bulinski, and G. G. Gundersen. 1991. Microtubule bundling in cells. *Nature.* 349:24.

20. Marx, A., J. Pless, E. M. Mandelkow, and E. Mandelkow . 2000. On the rigidity of the cytoskeleton: are MAPs crosslinkers or spacers of microtubules? *Cell. Mol. Biol.* 46:949–965.

21. Lee, G., and R. Brandt. 1992. Microtubule-bundling studies revisited: is there a role for MAPs. *Trends Cell Biol.* 2:286–289.

22. Asakura, S., and F. Oosawa. 1958. Interaction between particles suspended in solutions of macromolecules. *J. Polym. Sci. [B].* 33: 183–192.

23. Dogic, Z., and S. Fraden. 2001. Development of model colloidal liquid crystals and the kinetics of the isotropic-smectic transition. *Philisophical Transactions of the Royal Society of London.* 359:997–1014.

24. Adams, M., and S. Fraden. 1998. Phase behavior of mixtures of rods (tobacco mosaic virus) and spheres (polyethylene oxide, bovine serum albumin). *Biophys. J.* 74:669–677.

25. Bloomfield, V. 1996. DNA condensation. *Curr. Opin. Struct. Biol.* 6:334–341.

26. Hosek, M., and J. X. Tang. 2004. Polymer-induced bundling of F-actin and the depletion force. *Phys. Rev. E.* 69:051907.

27. Needleman, D. J., et al. 2004. Synchrotron x-ray diffraction study of microtubules buckling and bundling under osmotic stress: a probe of interprotofilament interactions. *Phys. Rev. Lett.* 93:198104.

28. Walter, H., and D. E. Brooks. 1995. Phase separation in cytoplasm, due to macromolecular crowding, is the basis for microcompartmentation. *FEBS Lett.* 361:135–139.

29. Parsegian, V. A., R. P. Rand, and D. C. Rau. 1995. Macromolecules and water: probing with osmotic stress. *Methods Enzymol.* 259:43–94.

30. Millman, B. M., T. C. Irving, B. G. Nickel, and M. E. Loosley-Millman. 1984. Interrod forces in aqueous gels of tobacco mosaic virus. *Biophys. J.* 45:551–556.

31. Rau, R. C., B. Lee, and V. A. Parsegian. 1984. Measurement of the repulsive force between polyelectrolyte molecules in ionic solution: hydration forces between parallel DNA double helices. *Proc. Natl. Acad. Sci. USA.* 81:2621–2625.

32. Dogic, Z., et al. 2004. Isotropic-nematic phase transition in suspensions of filamentous virus and the neutral polymer dextran. *Phys. Rev. E.* 69:051702.

33. Mason, T. G. 2002. Osmotically driven shape-dependent colloidal separations. *Phys. Rev. E.* 66:060402.

34. Kurz, J. C., and R. C. Williams. 1995. Microtubule-associated proteins and the flexibility of microtubules. *Biochemistry.* 34:13374–13380.

35. Gittes, F., B. Mickey, J. Nettleton, and J. Howard. 1993. Flexural rigidity of microtubules and actin filaments measured from thermal fluctuations in shape. *J. Cell Biol.* 120:923–934.

36. Mickey, B., and J. Howard. 1995. Rigidity of microtubules is increased by stabilizing agents. *J. Cell Biol.* 130:909–917.

37. Venier, P., A. C. Maggs, M. F. Carlier, and D. Pantaloni . 1994. Analysis of microtubule rigidity using hydrodynamic flow and thermal fluctuations. *J. Biol. Chem.* 269:13353–13360.

38. Felgner, H., R. Frank, J. Biernat, E. M. Mandelkow, E. Mandelkow, B. Ludin, A. Matus, and M. Schliwa. 1997. Domains of neuronal microtubule-associated proteins and flexural rigidity of microtubules. *J. Cell Biol.* 138:1067–1075.

39. Felgner, H., R. Frank, and M. Schliwa. 1996. Flexural rigidity of microtubules measured with the use of optical tweezers. *J. Cell Sci.* 109: 509–516.

40. Vinckier, A., C. Dumortier, Y. Engelborghs, and L. Hellemans. 1996. Dynamical and mechanical study of immobilized microtubules with atomic force microscopy. *Journal of Vacuum Science and Technology B.* 14:1427–1431.

41. de Pablo, P. J., I. A. Schaap, F. C. MacKintosh, and C. F. Schmidt. 2003. Deformation and collapse of microtubules on the nanometer scale. *Phys. Rev. Lett.* 91:098101.

42. Chretien, D., and S. D. Fuller. 2000. Microtubules switch occasionally into unfavorable configurations during elongation. *J. Mol. Biol.* 298:663–676.

43. Chretien, D., H. Flyvbjerg, and S. D. Fuller. 1998. Limited flexibility of the interprotofilament bonds in microtubules assembled from pure tubulin. *Eur. Biophys. J.* 27:490–500.

44. Janosi, I. M., D. Chretien, and H. Flyvbjerg. 2002. Structural microtubule cap: stability, catastrophe, rescue, and third state. *Biophys. J.* 83:1317–1330.

45. Janosi, I. M., D. Chretien, and H. Flyvbjerg. 1998. Modeling elastic properties of microtubule tips and walls. *Eur. Biophys. J.* 27: 501–513.

46. Arakawa, T., and S. N. Timasheff. 1982. Stabilization of protein structure by sugars. *Biochemistry.* 21:6536–6544.

47. Arakawa, T., and S. N. Timasheff. 1985. Mechanism of poly(ethylene glycol) interaction with proteins. *Biochemistry.* 24:6756–6762.

48. Lee, J. C., and L. L. Y. Lee. 1979. Interaction of calf brain tubulin with poly(ethylene glycols). *Biochemistry.* 18:5518–5526.

49. Herzog, W., and K. Weber. 1978. Microtubule formation by pure brain tubulin in vitro. The influence of dextran and poly(ethylene glycol). *Eur. J. Biochem.* 91:249–254

50. Fuller, N., and R. P. Rand. 1999. Water in actin polymerization. *Biophys. J.* 76:3261–3266.

51. Hitt, A. L., A. R. Cross, and R. C. Williams. 1990. Microtubule solutions display nematic liquid crystal structure. *J. Biol. Chem.* 265: 1639–1647.

52. Doi, M., and S. F. Edwards. 1986. The Theory of Polymer Dynamics. International Series of Monographs on Physics, Vol. 73. Clarendon Press, Oxford.

53. Andreu, J. M., J. Bordas, J. F. Diaz, J. Garcia de Ancos, R. Gil, F. J. Medrano, E. Nogales, E. Pantos, and E. Towns-Andrews. 1992. Low resolution structure of microtubules in solution. *J. Mol. Biol.* 226: 169–184.

54. Bordas, J., E. M. Mandelkow, and E. Mandelkow. 1983. Stages of tubulin assembly and disassembly studied by time-resolved synchrotron x-ray scattering. *J. Mol. Biol.* 164:89–135.

55. Needleman, D. J., M. A. Ojeda-Lopez, U. Raviv, H. P. Miller, L. Wilson, and C.R. Safinya. 2004. Higher order assembly of microtubules by counter-ions: from hexagonal bundles to living necklaces. *Proc. Natl. Acad. Sci. USA.* 101:16099–16103.

56. Als-Nielsen, J., and D. McMorrow. 2001. Elements of Modern X-Ray Physics. John Wiley & Sons, New York.

57. Kittel, C. 1995. Introduction to Solid State Physics. Wiley, Hoboken, NJ.

58. Curry, S., H. Mandelkow, P. Brick, and N. Franks. 1998. Crystal structure of human serum albumin complexed with fatty acid reveals an asymmetric distribution of binding sites. *Nat. Struct. Biol.* 5:827–835.

59. Santos, S. F., et al. 2003. A systematic study of bovine serum albumin (BSA) and sodium dodecyl sulfate (SDS) interactions by surface tension and small angle x-ray scattering. *J. Colloid Interface Sci.* 262: 400–408.

60. Giddings, J. C., et al. 1968. Statistical theory for the equilibrium distribution of rigid molecules in inert porous networks. Exclusion chromatography. *J. Phys. Chem.* 72:4397–4408.

61. Devanand, K., and J. C. Selser. 1991. Asymptotic-behavior and long-range interactions in aqueous-solutions of poly(ethylene oxide). *Macromolecules.* 24:5943–5947.

62. Nodmeier, E. 1993. Static and dynamic light-scattering solution behavior of pullulan and dextran in comparison. *J. Phys. Chem.* 97: 5770–5785.

63. Casassa, E. F. 1967. Equilibrium distribution of flexible polymer chains between a macroscopic solution phase and small voids. *J. Polym. Sci.* 5:773–778.

64. Daoud, M., and P. G. D. Gennes. 1977. Statistic of macromolecular solutions trapped in small pores. *J. Phys. [E].* 38:85–93.

65. Farrell, K. W., and L. Wilson. 1984. Tubulin-colchicine complexes differentially poison opposite microtubule ends. *Biochemistry*. 23: 3741–3748.

66. Li, Y. K., R. Edsall Jr., P. G. Jagtap, D. G. Kingston, and S. Bane. 2000. Equilibrium studies of a fluorescent paclitaxel derivative binding to microtubules. *Biochemistry*. 39:616–623.

67. Leckband, D., and J. Israelachvili. 2001. Intermolecular forces in biology. *Q. Rev. Biophys.* 34:105–267.

68. Baker, N. A., D. Sept, S. Joseph, M. J. Holst, and J. A. McCammon. 2001. Electrostatics of nanosystems: application to microtubules and the ribosome. *Proc. Natl. Acad. Sci. USA*. 98:10037–10041.

69. Strey, H. H., R. Podgornik, D. C. Rau, and V.A. Parsegian. 1998. DNA-DNA interactions. *Curr. Opin. Struct. Biol.* 8:309–313.

70. Howard, J. 2001. Mechanics of Motor Proteins and the Cytoskeleton. Sinauer Associates, Sunderland, MA.

71. Ventsel, E., and T. Krauthammer. 2001. Thin Plates and Shells. Marcel Dekker, Inc., New York.

72. Sept, D., N. A. Baker, and J. A. Mccammon. 2003. The physical basis of microtubule structure and stability. *Protein Sci.* 12:2257–2261.

73. Keskin, O., S. R. Durell, I. Bahar, R. L. Jernigan, and D. G. Cove. 2002. Relating molecular flexibility to function: a case study of tubulin. *Biophys. J.* 83:663–680.

74. Stukalin, E. B., and A. B. Kolomeisky. 2004. Simple growth models of rigid multifilament biopolymers. *J. Chem. Phys.* 121:1097–1104.

75. Landau, L. D., and E. M. Lifshitz. 2000. Theory of Elasticity. Butterworth-Heinemann, Oxford.

76. Schaap, I. A. T., P. J. de Pablo, and C. F. Schmidt. 2004. Resolving the molecular structure of microtubules under physiological conditions with scanning force microscopy. *Eur. Biophys. J.* 33:462–467.

77. Chan, S. P., et al. 2003. Carbon nanotube bundles under high pressure: transformation to low-symmetry structures. *Phys. Rev. B*. 68:075404.

78. Elliot, J. A., et al. 2004. Collapse of single-wall carbon nanotubes is diameter dependent. *Phys. Rev. Lett.* 92:095501.

79. Lorman, V., R. Podgornik, and B. Zeks. 2001. Positional, reorientational, and bond orientational order in DNA mesophases. *Phys. Rev. Lett.* 87:218101.

80. Zhang, X. H., Z. F. Liu, and X. G. Gong. 2004. Comment on ''Collapse of single-wall carbon nanotubes is diameter dependent''. *Phys. Rev. Lett.* 93:149601.

81. Dogterom, M., and B. Yurke. 1997. Measurement of the force-velocity relation of growing microtubules. *Science*. 278:856–860.

82. Krasilnikov, O. V., and S. M. Bezrukov. 2004. Polymer partitioning from nonideal solutions into protein voids. *Macromolecules*. 37:2650–2657.

83. Bray, D. 2001. Cell Movements. Garland, New York.

84. Rieder, C., and A. S. Bajer. 1977. Heat-induced reversible hexagonal packing of spindle microtubules. *J. Cell Biol.* 74:717–725.